Research Square

Preprints are preliminary reports that have not undergone peer review.
They should not be considered conclusive, used to inform clinical practice,
or referenced by the media as validated information.

# From phytochemical prioritization to cell-based validation: tricoumaroyl spermidine from Agrimonia eupatoria displays cell-context-dependent antiproliferative activity associated with PI3K/AKT/mTOR-HIF-1α signaling

**Hayarpi Javrushyan**
Yerevan State University
**Meri Kocharyan**
Yerevan State University
**Arpine Hakobyan**
Yerevan State University
**Aqsanna Gevorgyan**
Yerevan State University
**Nikolay Avtandilyan**
nv.avtandilyan@ysu.am
Yerevan State University
**Alina Maloyan**
Knight Cardiovascular Institute, Oregon Health & Science University
**Mikayel Ginovyan**
Yerevan State University

**Research Article**

**Keywords:** Agrimonia eupatoria, tricoumaroyl spermidine, PI3K/AKT/mTOR, HIF-1α, breast cancer, MCF-7, MDA-MB-231, A549, real-time cell analysis, KEGG enrichment

**Posted Date:** November 20th, 2026

**DOI:** https://doi.org/10.21203/rs.3.rs-10594229/v1

**License:** This work is licensed under a Creative Commons Attribution 4.0 International License.
Read Full License

**Additional Declarations:** No competing interests reported.

# Abstract

### Background

*Agrimonia eupatoria* L. is a medicinal plant with reported anticancer activity. Tricoumaroyl spermidine (TCS), a major constituent of its ethanolic extract (AEE), was previously identified as a potential regulator of PI3K signaling based on phytochemical and computational analyses. However, the biological activity of isolated TCS has not been experimentally validated. This study investigated the anticancer effects of purified TCS using AEE as a botanical comparator.

### Methods

The effects of AEE and TCS were evaluated in MCF-7 and MDA-MB-231 breast cancer cells by endpoint viability assays, real-time impedance monitoring, fluorescence-based live/dead cell imaging, and quantitative analysis of live and dead cell populations. The effects of TCS on breast cancer cell migration were assessed in MDA-MB-231 cells. Immunocytochemistry was performed to evaluate pPI3K, pAKT, mTOR, HIF-1α, and Caspase-3 expression in insulin- and $CoCl_2$-stimulated A549 and MDA-MB-231 cells. Molecular docking, protein-protein interaction, and KEGG pathway enrichment analyses were performed to identify potential molecular targets and associated signaling pathways.

### Results

AEE reduced the viability of MCF-7 cells in a time- and concentration-dependent manner, whereas MDA-MB-231 cells were comparatively less sensitive in endpoint assays. TCS decreased cell proliferation and increased the proportion of membrane-compromised cells in MCF-7 cultures. In MDA-MB-231 cells, AEE significantly reduced proliferation, whereas TCS had little effect on proliferation but significantly inhibited cancer cell migration and increased the proportion of membrane-compromised cells. Under insulin/hypoxic stimulation, TCS reduced pPI3K, pAKT, mTOR, and HIF-1α immunofluorescence signals while increasing Caspase-3 staining. Molecular docking predicted the strongest binding of TCS to COX-2 and AKT, and pathway enrichment analysis linked the candidate targets to apoptosis, PI3K/Akt, HIF-1, p53, autophagy, VEGF, TNF, JAK/STAT, MAPK, and mTOR signaling.

### Conclusions

TCS exhibited anticancer activity with distinct effects depending on the breast cancer cell type, suppressing proliferation in MCF-7 cells and inhibiting migration in MDA-MB-231 cells. The computational and immunocytochemical findings support the involvement of PI3K/AKT/mTOR/HIF-1α-associated signaling, although direct target engagement remains to be confirmed. These findings identify TCS as a promising natural-product lead for further mechanistic and in vivo studies.


# 1. Introduction

Cancer remains a major global health burden, with an estimated 20.6 million new cases and 9.8 million cancer-related deaths worldwide in 2024 - based on population growth and ageing alone, the annual number of new cases is projected to reach 34.4 million by 2050, representing a 67% increase [1]. Despite major advances in targeted therapy and immunotherapy, tumor heterogeneity, adaptive signaling, metastatic dissemination, and treatment resistance continue to limit durable clinical responses. These constraints sustain interest in natural products both as chemically diverse sources of lead compounds and as tools for identifying multi-node vulnerabilities in oncogenic signaling networks.

The PI3K/AKT/mTOR pathway is one of the most frequently dysregulated survival networks in human cancer. It coordinates cell growth, metabolism, protein synthesis, stress adaptation, and resistance to apoptosis, and it is especially relevant in breast and lung malignancies [2]. PI3K/AKT/mTOR signaling also intersects with hypoxia-inducible factor-1α (HIF-1α), thereby linking growth-factor signaling to glycolytic reprogramming, angiogenesis, invasion, and treatment resistance [3, 4]. Because these processes are connected rather than linear, phenotypic and network-level analyses are useful for generating mechanistic hypotheses, provided that they are not presented as substitutes for direct target-engagement experiments.

*Agrimonia eupatoria* L. (Rosaceae), commonly known as common agrimony, is a phenolic-rich medicinal plant with a long history of traditional use. Modern phytochemical studies have identified flavonoids, phenolic acids, tannins, ellagitannins, and other specialized metabolites in Agrimonia eupatoria, while its extracts have demonstrated antioxidant, anti-inflammatory, antimicrobial, and cytotoxic activities [5]. More recently, our comprehensive LC-Q-Orbitrap HRMS profiling of an Armenian A. eupatoria ethanolic extract annotated 112 phenolic constituents-including flavan-3-ols, hydroxycinnamic acids, flavonols, flavones, and ellagitannins-and identified tricoumaroyl spermidine as a promising candidate bioactive compound [6]. At the constituent level, agrimoniin has been reported to induce apoptosis through ROS-linked metabolic disruption and to inhibit AKT/ERK signaling in pancreatic cancer models [7, 8]. These observations support the anticancer relevance of the genus but also emphasize that distinct *Agrimonia* metabolites can produce different mechanisms and phenotypes.

Our previous study established the starting point for the present work. Using an Armenian *A. eupatoria* ecotype, we showed that AEE exerted context-dependent cytotoxic and pro-oxidant effects and suppressed total and phosphorylated PI3K together with downstream AKT/mTOR, HIF-1α, COX-2, and MMP-2-associated readouts in A549 cells. LC-Q-Orbitrap HRMS profiling identified TCS in the extract, and docking prioritized it as a putative PI3K-interacting lead [6]. In that study, TCS was identified as a putative contributor to the anticancer activity of *A. eupatoria* and prioritized as a cancer-relevant PI3K-targeting candidate. However, this association remained inferential, as pathway modulation was demonstrated for the crude extract, whereas isolated TCS had not yet been experimentally evaluated in cancer cell models.

TCS is a hydroxycinnamoyl spermidine conjugate rather than free spermidine. This distinction is biologically important. Tricoumaroyl-spermidine isolated from rose has been reported to protect HepG2

cells from ethanol-induced apoptosis [9], demonstrating that its effects can depend on the cellular stress model. Moreover, recent work indicates that endogenous spermidine production can support basal-like breast cancer aggressiveness through the AMD1-eIF5A hypusination-TCF4 axis [10]. These findings do not predict the behavior of the chemically conjugated TCS molecule, but they reinforce the need for direct, cell-context-specific validation rather than extrapolation from the parent polyamine or from in silico binding predictions.

Accordingly, the present study was designed as a continuation and validation study. We tested isolated TCS across complementary phenotypic assays in luminal MCF-7 and triple-negative MDA-MB-231 breast cancer cells and evaluated pathway-associated markers in A549 and MDA-MB-231 cells under growth-factor and chemical hypoxia stimulation. AEE was included as a botanical comparator, not as a dose-equivalent source of TCS. Molecular docking, protein-interaction mapping, and KEGG pathway enrichment were used to contextualize - not prove - the candidate mechanism. The central question was whether a compound previously prioritized from AEE exhibits reproducible anticancer-associated activity when tested directly as an isolated molecule.

## 2. Materials and Methods

## 2.1. Study design and interpretive framework

This study combined phenotypic, pathway-associated, and computational analyses to evaluate TCS as an *A. eupatoria*-derived lead. AEE served as a botanical reference, and dactolisib (NVP-BEZ235) served as a pharmacological reference inhibitor of PI3K/mTOR signaling. Extract-compound comparisons were interpreted as functional comparisons under the tested conditions and not as evidence of dose equivalence, synergy, or attribution of the whole-extract effect to TCS.

## 2.2. Chemicals, reagents, antibodies, and reference compounds

Cell-culture reagents and chemicals used in the breast cancer cell experiments were purchased from Sigma-Aldrich (St. Louis, MO, USA), Agilent Technologies (Santa Clara, CA, USA), and Abcam (Cambridge, UK), unless otherwise specified. Primary antibodies used for immunocytochemistry/immunofluorescence included anti-HIF-1α (ab179483), anti-β-actin (ab8227), anti-phospho-PI3K (ab191606), anti-phospho-AKT (ab179463), anti-mTOR, and anti-caspase-3. Goat anti-rabbit IgG H&L secondary antibodies conjugated to Alexa Fluor 488 (ab150077) were obtained from Abcam.

Tricoumaroyl spermidine (TCS) (Sigma) was evaluated as the isolated candidate compound prioritized in our previous LC-Q-Orbitrap HRMS and molecular-docking study. Dactolisib (NVP-BEZ235), a dual PI3K/mTOR inhibitor, was used as a pharmacological reference compound in the real-time cell analysis and fluorescence live/dead assays.

## 2.3. Plant material and extract preparation

The plant material and extract corresponded to the *A. eupatoria* preparation characterized previously [6]. Aerial parts were collected during flowering in June 2023 near Navur village, Tavush region, Armenia (1400–1550 m above sea level), on privately owned land with the permission of the landowner. Formal botanical identification of the plant material was undertaken by Dr. Narine Zakaryan (Department of Botany and Mycology, Yerevan State University, Armenia), and a voucher specimen was deposited in the Yerevan State University Herbarium (voucher no. ERCB13207). Dried aerial material was macerated with 96% ethanol at a 1:10 (w/v) ratio at 2–8°C for 24 h, with three extraction cycles. A stock equivalent to 50 mg dry extract/mL was prepared; the extraction yield was 15.4 ± 0.28% based on dry-residue determination [6].

## 2.4. Cell culture

Human breast adenocarcinoma MCF-7 cells (ATCC HTB-22), triple-negative breast cancer MDA-MB-231 cells (ATCC HTB-26), and human lung adenocarcinoma A549 cells (ATCC CCL-185) were obtained from the American Type Culture Collection (ATCC, Manassas, VA, USA). Cells were maintained in Dulbecco's modified Eagle's medium (DMEM) supplemented with 2 mmol/L L-glutamine, 200 mg/L sodium pyruvate, 10% fetal bovine serum, 100 U/mL penicillin, and 100 µg/mL streptomycin. MCF-7 cultures were additionally supplemented with 10 µg/mL human recombinant insulin. Cells were maintained at 37°C in a humidified atmosphere containing 5% $CO_2$ using a PHCbi MCO-230AICUVL-PA $CO_2$ incubator. Cultures were regularly screened for mycoplasma contamination using the Universal Mycoplasma Detection Kit (ATCC, Manassas, VA, USA). Cells were subcultured before reaching complete confluence, and only cultures showing normal morphology and growth characteristics were used for experiments.

## 2.5. MTT-based cell-viability analysis

The metabolic activity of MCF-7 and MDA-MB-231 cells following exposure to *A. eupatoria* ethanolic extract was determined using the 3-(4,5-dimethylthiazol-2-yl)-2,5-diphenyltetrazolium bromide (MTT) reduction assay. Cells were exposed to AEE at concentrations ranging from 0 to 0.5 mg/mL for 4, 24, or 72 h. Vehicle-control cells received the corresponding volume of extraction solvent, resulting in a final ethanol concentration of 1% (v/v). The same vehicle concentration was maintained across the corresponding treatment and control groups. Following treatment, MTT reduction was measured according to the previously established protocol [11]. Cell viability was calculated relative to the corresponding vehicle-treated control, which was defined as 100%. Each experiment was performed independently three times, with four technical replicate wells per treatment condition in each experiment. Results are presented as the mean ± SEM of three independent biological experiments.

## 2.6. Real-time impedance monitoring and live/dead imaging

Real-time changes in cell behavior were recorded with the xCELLigence RTCA eSight platform (Agilent Technologies) using E-Plate 96 plates. For background correction, 50 µL of cell-free complete DMEM

was dispensed into each well before impedance measurement. MCF-7 and MDA-MB-231 cells were then seeded at 1 × $10^4$ cells/well in 150 µL of complete medium, giving a final volume of 200 µL. After 30 min at room temperature to promote uniform settling, plates were transferred to 37°C and 5% $CO_2$ for a 24-h attachment period. Cells were subsequently exposed to AEE (0.5 mg/mL), TCS (50 µM), dactolisib (0.2 µM), or the corresponding vehicle control.

Cell index was collected at 15-min intervals for up to 96 h, with treatment addition defined as the start of the post-treatment analysis period. E-Live Red and E-Tox Green reagents were introduced with the treatments at their final working concentrations, and fluorescence images were acquired in parallel with impedance measurements using the red and green channels of the RTCA eSight system. Treatment solutions and fluorescent probes were prepared in complete medium so that the final culture volume remained 200 µL/well. Areas under the cell-index curves were calculated over the predefined post-treatment interval. Each condition was evaluated in replicate wells in three independent experiments, and results are presented as mean ± SEM.

To complement the representative fluorescence images, object-level mean fluorescence intensities at 72 h were visualized as bivariate scatter plots, with E-Live Red mean intensity on the x-axis and E-Tox Green mean intensity on the y-axis. Quadrant thresholds were applied within each cell line to operationally classify objects as Red+/Green− (live-like), Red+/Green+ (dual-positive), Red−/Green+ (green-dominant), or Red−/Green− (low-signal/debris). The proportion of total gated objects in each quadrant was calculated. Because these categories are based on fluorescence intensity and membrane integrity, they were interpreted as cell-state or cytotoxicity-associated profiles rather than definitive stages of apoptosis. Representative plots from three independent experiments are presented.

## 2.7. Real-time migration assay

Migration-associated impedance was measured with an xCELLigence RTCA DP instrument and uncoated CIM-Plate 16 assemblies. The lower compartments received 150 µL of medium containing 10% fetal bovine serum as the chemotactic stimulus. MDA-MB-231 cells were resuspended in medium containing 1% fetal bovine serum and added to the upper compartments at 5 × $10^4$ cells/well. The test conditions comprised AEE (0.5 mg/mL), TCS (50 µM), dactolisib (0.2 µM), and the corresponding vehicle control.

After assembly, the plates were maintained at 37°C, and impedance was recorded every 15 min for 24 h. The RTCA software converted impedance changes into cell-index values, and cumulative migration was summarized as the area under the 24-h curve. Each condition was analyzed in triplicate in three biologically independent experiments; data are reported as mean ± SEM.

## 2.8. Immunocytochemical analysis of pathway-associated markers

A549 and MDA-MB-231 cells were seeded in black, clear-bottom 96-well cell-culture plates and incubated for 24 h before treatment. To induce hypoxia-associated signaling, cells were exposed to

$CoCl_2$ at a final concentration of 200 μM. Insulin at 200 nM was used to stimulate PI3K/AKT-associated signaling. Cells were treated with TCS at 50 μM, either alone or in combination with the indicated stimulatory conditions, and incubated for 20 h before fixation.

Following treatment, cells were fixed with 4% paraformaldehyde, permeabilized with 1% Triton X-100, and blocked with 1% bovine serum albumin. Cells were incubated overnight at 4°C with primary antibodies against phospho-PI3K, phospho-AKT, mTOR, HIF-1α, or Caspase-3, each diluted 1:250. After washing, cells were incubated with goat anti-rabbit IgG H&L secondary antibodies conjugated to Alexa Fluor 488 or Alexa Fluor 647 at a dilution of 1:500. Nuclei were counterstained with DAPI.

Images were acquired at room temperature using a Cytation C10 confocal imaging reader equipped with a 20× objective and controlled using Gen5 software [6]. Eight fields of view were acquired per well. Average fluorescence intensity was quantified using Gen5 software after application of identical acquisition and analysis settings to all experimental groups. Fluorescence values were background-corrected and normalized to the untreated control. Data were obtained from three independent experiments and are presented as mean ± SEM.

# 2.9. Molecular docking analysis

*Protein structure retrieval and preparation*

The present molecular docking analysis was conducted independently of the PI3K-focused computational study reported previously [6]. In that earlier study, TCS was docked within the ATP-competitive binding pocket of PI3K using PDB structure 6C1S and yielded an AutoDock Vina score of approximately − 9.4 kcal/mol. In the present study, TCS was evaluated in separate target-specific docking analyses against AKT, PI3K, mTOR, COX-2, MMP-2, Bcl-2, and Caspase-3. Three-dimensional structures of AKT (PDB ID: 6CCY), PI3K (PDB ID: 4OVV), mTOR (PDB ID: 4JT5), Bcl-2 (PDB ID: 4MAN), COX-2 (PDB ID: 1CX2), MMP-2 (PDB ID: 8H78), and Caspase-3 (PDB ID: 2XYG) were retrieved from the Protein Data Bank (https://www.rcsb.org/). Receptor structures were inspected and prepared using the PyMOL Molecular Graphics System (Schrödinger, LLC). Crystallographic water molecules, co-crystallized ligands, and non-essential heteroatoms were removed before docking. Catalytically or structurally relevant metal ions and cofactors were retained where required by the corresponding receptor structure and docking model.

*Docking simulations and interaction analysis*

TCS was docked against each selected protein target using AutoDock Vina [12]. The exhaustiveness parameter was set to 16 to increase conformational sampling within the predefined binding regions. The resulting AutoDock Vina scores were used to characterize the predicted TCS-protein interactions under the applied target-specific conditions and were not interpreted as experimentally determined binding affinities. The predicted TCS-protein complexes were inspected in PyMOL, and two-dimensional interaction maps were generated using BIOVIA Discovery Studio Visualizer. Hydrogen bonds,

hydrophobic contacts, π-mediated interactions, van der Waals contacts, and unfavorable interactions were recorded to characterize the predicted positioning of TCS within the respective binding pockets.

## 2.10. Protein-interaction network and KEGG pathway contextualization

*Protein-protein interaction network analysis*

Proteins experimentally evaluated by immunocytochemistry (ICC), including PIK3CA, AKT1, MTOR, CASP3, and HIF1A, were used as seed proteins for protein-protein interaction analysis. Functional associations among these proteins and their interacting partners were identified using the STRING database (version 12.0) with Homo sapiens selected as the reference organism. The generated interaction network was imported into Cytoscape (version 3.10.3) for visualization [13]. Proteins measured by ICC were highlighted as colored nodes, whereas additional interacting proteins identified by STRING were displayed as gray nodes. Network analysis was performed to explore the functional relationships between signaling pathways involved in cell survival, apoptosis, hypoxia, and tumor progression.

*KEGG pathway enrichment analysis*

KEGG pathway enrichment analysis was performed using the Enrichr web platform (https://maayanlab.cloud/Enrichr/). The predefined gene set (PIK3CA, AKT1, CASP3, HIF1A, MTOR, TP53, BCL2, BAX, CASP9, MMP2, SLC2A1, and PTGS2) was submitted as official gene symbols and evaluated against the KEGG 2026 Human library. Pathways were ranked according to the adjusted P value, and selected biologically relevant pathways were visualized as a bubble plot using the SRplot online platform [14].

## 2.11. Statistical analysis

Statistical analyses were conducted in GraphPad Prism 8. Technical replicate wells were averaged within each experiment, so that each independent experiment constituted the statistical unit. Data are expressed as mean ± SEM unless a figure legend specifies otherwise. Distributional assumptions were assessed before group comparisons. Normally distributed multi-group data were analyzed by one-way ANOVA followed by Dunnett's test for comparisons with a single control or Tukey's test for pairwise comparisons; the Kruskal-Wallis test with an appropriate multiple-comparison procedure was used when parametric assumptions were not satisfied. RTCA proliferation and migration datasets were compared using AUC values calculated separately for each independent experiment. MTT concentration-response curves were fitted with a four-parameter variable-slope model where the data adequately defined the response. All tests were two-sided, and $P < 0.05$ was considered statistically significant.

# 3. Results

# 3.1. Docking analysis identifies multiple candidate TCS-protein interactions and contextualizes the target network

TCS was evaluated in independent target-specific docking analyses against six cancer-associated proteins: AKT, PI3K, mTOR, COX-2, MMP-2, Bcl-2, and Caspase-3 (Figure 1). Under the applied computational conditions, AutoDock Vina scores were -8,395 kcal/mol for mTOR, −8.947 kcal/mol for COX-2, −8.483 kcal/mol for AKT, −6.888 kcal/mol for MMP-2, −5.751 kcal/mol for PI3K, −5.061 kcal/mol for Bcl-2, and −4.361 kcal/mol for Caspase-3 (Figure 1). Because target-specific receptor structures and binding-site definitions were used, these numerical values should not be interpreted as a definitive cross-target affinity ranking.

Inspection of the predicted binding poses revealed distinct interaction patterns for TCS within the respective protein-binding pockets. In the AKT complex, TCS formed predicted conventional hydrogen bonds with Asp292 and Thr195. π-Sigma interactions were observed with Ile186 and Val164, while π-alkyl contacts involved Leu181, Leu156, and Ala177. A π-π T-shaped interaction was identified with Phe161. Additional van der Waals contacts involved Glu191, His194, Lys158, Gly159, Gly294, Lys179, Glu234, Tyr229, Ala230, Phe438, Leu295, and Met281.

Within the PI3K binding pocket, TCS formed predicted conventional hydrogen bonds with Gln721, Asn803, Cys844, and Val843. Carbon-hydrogen bond interactions were observed involving Ser6, Asp717, Gly804, and Pro5. An unfavorable donor-donor interaction was identified with Lys720, while additional van der Waals contacts involved Gly842, Ile841, Ile713, His676, and neighboring residues. Because the present PI3K docking experiment used a computational setup distinct from that employed in the earlier PI3K-focused study, the resulting pose and score should be interpreted within the current receptor model.

Within the mTOR binding pocket, TCS established two predicted conventional hydrogen bonds with Arg2251 and Asp2195, as well as a carbon-hydrogen bond with Ser2342. Hydrophobic stabilization was further supported by a π-sigma interaction with Ile2237, a π-π stacked interaction with Trp2239, and a π-sulfur interaction involving Met2345. Additional alkyl and π-alkyl contacts were observed with Ala2248, Pro2169, and Ile2356, while Asp2357 and neighboring residues contributed through van der Waals interactions. Collectively, these non-covalent interactions indicate stable accommodation of TCS within the predicted ATP-binding pocket of mTOR.

The predicted TCS-MMP-2 complex was stabilized predominantly by aromatic and hydrophobic interactions. A π-sigma interaction was observed with Leu138, while π-π stacked interactions involved His121, His125, and Tyr74. Alkyl and π-alkyl interactions were detected with Leu117, Leu83, and Leu138. Additional van der Waals contacts involved Thr146, Thr144, Ala140, Tyr143, Ile142, Ala84, Ala86, Phe5, Glu130, His85, His131, Leu82, Phe87, Val118, Ala137, and Phe149.

In the Bcl-2 binding pocket, TCS formed a predicted conventional hydrogen bond with Ala97. π-π stacked interactions were observed with Phe101 and Tyr199, whereas a π-π T-shaped interaction involved Tyr105. π-Alkyl contacts were detected with Ala146, Met112, and Val145. An unfavorable acceptor-acceptor interaction was observed with Asp100. Additional van der Waals contacts involved Arg104, Gly142, Trp141, Phe195, Phe150, Val153, Glu149, Phe109, Asp108, Leu134, and neighboring residues within the binding pocket.

Within the Caspase-3 binding pocket, TCS formed predicted conventional hydrogen bonds with Cys163 and Tyr204. A π-sigma interaction was observed with Thr166, while π-π stacking involved His121. A π-sulfur interaction was also identified with Cys163. An unfavorable acceptor-acceptor contact involved Gly165. Additional van der Waals interactions were detected with Thr59, Met61, Gly122, Phe128, Glu123, Thr62, Gly60, and neighboring residues.

In the COX-2 binding pocket, TCS formed predicted conventional hydrogen bonds with Gln192 and Gln350, together with a carbon-hydrogen bond involving Gly193. A π-cation interaction was identified with Lys511, while alkyl and π-alkyl contacts involved Pro514, His95, Tyr355, and Arg513. An unfavorable donor-donor interaction was observed with Asn581. Additional van der Waals contacts involved His90, Tyr91, Thr94, Asp515, Ala516, Pro191, His356, Gly354, Ser353, Asn87, and neighboring residues within the binding region.

Collectively, these docking results identify several experimentally testable TCS-protein interaction hypotheses. The predicted AKT, PI3K, and mTOR interactions are relevant to the PI3K/AKT/mTOR-associated cellular findings, while the MMP-2 and COX-2 complexes provide potential links to migration- and inflammation-related processes. However, the docking analysis does not establish direct binding, enzymatic inhibition, cellular target engagement, or preferential target affinity.

The protein-protein interaction network revealed extensive functional connectivity among the PI3K/AKT/mTOR core, HIF1A, apoptosis-associated regulators including TP53, BCL2, BAX, CASP9, and CASP3, and migration- and inflammation-associated proteins including MMP2 and PTGS2 (Figure 2A). AKT1 and CASP3 appeared centrally positioned within the visualized network, whereas PIK3CA, MTOR, and HIF1A connected survival signaling with metabolic and hypoxia-associated nodes.

## 3.2. AEE and TCS exert time-dependent antiproliferative and cytotoxic effects on MCF-7 cells

The effects of *A. eupatoria* ethanolic extract (AEE) and isolated tricoumaroyl spermidine on MCF-7 breast adenocarcinoma cells were evaluated using endpoint viability analysis, real-time impedance monitoring, and fluorescence-based live/dead imaging (Figure 2).

AEE reduced MCF-7 cell viability in a concentration- and time-dependent manner (Figure 2A). After 4 h of exposure, viability remained close to the control level across most of the tested concentration range,

indicating limited short-term activity. A greater reduction was observed after 24 h, while the strongest response occurred after 72 h. At the longest exposure time, the concentration-response curve crossed the 50% viability threshold at approximately 0.25-0.30 mg/mL. These findings indicate that sustained exposure is required for AEE to produce its maximal effect in MCF-7 cells. However, the endpoint assay alone cannot distinguish between reduced proliferation, loss of viability, altered metabolic activity, or a combination of these effects.

Real-time impedance analysis provided complementary information on treatment-associated changes in cell growth, attachment, morphology, and viability (Figure 2B). Vehicle-treated MCF-7 cells showed a progressive increase in cell index throughout the monitoring period, consistent with continued cell accumulation and stable adhesion. Dactolisib produced the strongest suppression of the cell-index trajectory and the lowest cumulative area under the curve, with an AUC of approximately 100 and a significant reduction relative to the control ($p < 0.001$).

TCS caused a sustained divergence from the control trajectory and significantly reduced the cumulative cell-index AUC (Figure 2B) to approximately 155 ($p < 0.01$ versus control). AEE produced an intermediate response, with an AUC of approximately 215; however, its difference from the control did not reach statistical significance under the tested RTCA conditions. These kinetic results demonstrate measurable activity of isolated TCS in MCF-7 cells. Because impedance-derived cell index reflects a composite of cell number, attachment, morphology, and viability, the reduction should not be interpreted exclusively as inhibition of proliferation.

The ratio of live to dead cells was determined by scatter plot analysis of cells stained with the fluorescent dyes eLive Red and eTox Green. Fluorescence imaging and object-level scatter analysis were consistent with the impedance findings (Figure 2C, D). Control cultures exhibited predominantly E-Live Red fluorescence with minimal E-Tox Green staining, indicating preservation of plasma-membrane integrity. In the representative control scatter plot, 44.03% of gated objects were in the live-like Red+/Green− quadrant, 6.19% were dual-positive, 5.31% were green-dominant, and 44.47% were classified as low-signal/debris. TCS treatment produced a pronounced redistribution, with the dual-positive fraction increasing to 60.70% and the green-dominant fraction to 8.34%, while the live-like fraction decreased to 8.10%. Dactolisib produced the strongest cytotoxicity-associated profile, with 59.89% dual-positive and 24.13% green-dominant objects and only 3.62% in the live-like quadrant. AEE produced a milder shift, with 10.36% dual-positive, 4.52% green-dominant, and 29.89% live-like objects. These fluorescence-defined distributions support treatment-associated membrane compromise but do not establish early or late stages of apoptosis. Taken together, the endpoint, kinetic, fluorescence-imaging, and object-level scatter analyses demonstrate that isolated TCS has reproducible antiproliferative- and cytotoxicity-associated activity in MCF-7 cells. AEE also reduced endpoint viability and altered fluorescence-based viability patterns, although its effect in the RTCA assay was weaker and did not reach statistical significance at the tested concentration. These findings validate TCS as a biologically active *A. eupatoria*-derived candidate compound but do not establish that it is the principal constituent responsible for the activity of the crude extract.

# 3.4. TCS suppresses migration-associated impedance and alters fluorescence-defined cell-state distributions in MDA-MB-231 cells without reducing proliferation-associated impedance

MDA-MB-231 cells showed a response pattern distinct from that observed in MCF-7 cells (Figure 3). In the endpoint viability assay, AEE produced only limited cytotoxicity in this cell line: cell viability remained close to control levels after 4 and 24 h of exposure, and after 72 h the highest tested concentration (0.5 mg/mL) reduced viability only to approximately 75% of control, without reaching the $IC_{50}$ threshold (Figure 3A).

Real-time impedance monitoring demonstrated that AEE, but not TCS, affected proliferation-associated cell behavior in MDA-MB-231 cells (Figure 3B). Dactolisib produced the strongest reduction in the cell-index trajectory and the lowest AUC. AEE also significantly reduced the cumulative cell-index AUC relative to untreated cells, supporting considerable antiproliferative activity under the tested conditions. In contrast, the TCS trajectory closely followed that of the control group, and its AUC did not differ significantly from control.

The fluorescence-based readouts revealed a more complex response (Figure 3C, E). Representative micrographs showed substantial E-Live Red fluorescence in TCS-treated cultures; however, object-level scatter analysis demonstrated a pronounced redistribution of gated objects. In the control plot, 30.65% of objects were live-like, 8.07% were dual-positive, 7.04% were green-dominant, and 54.24% were low-signal/debris. Following TCS treatment, the live-like fraction decreased to 6.59%, whereas the dual-positive and green-dominant fractions increased to 45.98% and 20.64%, respectively. Dactolisib produced 73.58% dual-positive and 10.74% green-dominant objects, with only 3.69% remaining in the live-like quadrant. AEE produced an intermediate shift, with 15.08% dual-positive, 16.27% green-dominant, and 15.15% live-like objects. Thus, although TCS did not reduce proliferation-associated impedance, the scatter analysis indicated a substantial membrane-compromise-associated fluorescence shift. These readouts assess different aspects of cell state and should not be treated as interchangeable.

Despite the limited effects of TCS on proliferation and viability, TCS significantly reduced migration-associated impedance in the real-time migration assay (Figure 3D). Untreated cells displayed the highest migration-associated cell-index trajectory, whereas dactolisib, AEE, and TCS showed lower trajectories throughout the monitoring period. AUC analysis confirmed the migration-inhibitory effect of TCS relative to untreated cells. Because the assay measures impedance associated with cell movement through the membrane, these findings support inhibition of migration-associated behavior but do not by themselves establish inhibition of invasion or metastasis.

Collectively, these results support a cell-context-dependent and assay-dependent TCS phenotype. In MDA-MB-231 cells, TCS did not reduce proliferation-associated impedance, but it altered the fluorescence-defined cell-state distribution and significantly reduced migration-associated impedance. AEE, by contrast, exerted measurable antiproliferative activity in this model. The divergence between the impedance and fluorescence readouts suggests that TCS may produce membrane-integrity changes in a detected cell subpopulation without a commensurate reduction in the cumulative impedance signal. This interpretation requires confirmation using orthogonal viability, apoptosis, and membrane-integrity assays, together with independent migration and invasion measurements.

## 3.5. TCS is associated with reduced PI3K/AKT/mTOR-HIF-1α signaling and increased Caspase-3 staining under stimulated conditions

Immunocytochemical analysis was performed to examine the effects of TCS on PI3K/AKT/mTOR-associated signaling, HIF-1α accumulation, and Caspase-3 immunoreactivity in A549 lung adenocarcinoma and MDA-MB-231 triple-negative breast cancer cells under combined growth-factor and chemical hypoxia stimulation.

To mimic a tumor-like microenvironment characterized by growth factor stimulation and hypoxic stress, A549 cells were co-treated with insulin (Ins; 200 nM) and $CoCl_2$ (200 μM) [15, 16]. Insulin was used as an activator of PI3K/AKT signaling, whereas $CoCl_2$ served as a chemical hypoxia mimetic by stabilizing HIF-1α and reproducing key aspects of hypoxic conditions. In A549 cells, combined treatment with insulin (Ins; 200 nM) and $CoCl_2$ (200 μM) increased the fluorescence intensity of the PI3K/AKT/mTOR pathway markers relative to untreated controls. Quantitative analysis showed an approximately 2.8-fold increase in pPI3K, a greater than twofold increase in pAKT, and an approximately 50% increase in mTOR-associated fluorescence (Figure 4A-C, I). These findings indicate activation of PI3K/AKT/mTOR-associated signaling under the applied stimulatory conditions. Treatment with TCS (50 μM) markedly attenuated these responses, reducing pPI3K fluorescence toward basal levels and significantly decreasing pAKT and mTOR signals relative to the Ins/$CoCl_2$-stimulated group.

HIF-1α immunoreactivity showed a similar response pattern in A549 cells (Figure 4D, I). $CoCl_2$ alone increased HIF-1α fluorescence relative to untreated controls, whereas combined Ins/$CoCl_2$ stimulation produced a greater increase. Addition of TCS significantly reduced HIF-1α accumulation under the stimulated condition. These observations are consistent with attenuation of growth- and hypoxia-associated signaling, although they do not establish whether TCS directly affects HIF-1α stabilization or acts indirectly through upstream signaling pathways.

Caspase-3-associated fluorescence displayed an inverse pattern relative to the survival-associated markers (Figure 4E, I). TCS alone increased Caspase-3 immunoreactivity to approximately twofold above the untreated control. Under combined Ins/$CoCl_2$ stimulation, subsequent TCS treatment also

significantly increased Caspase-3 staining relative to the stimulated group. This response is consistent with an apoptosis-associated shift; however, unless the antibody specifically recognizes cleaved Caspase-3, increased staining should not be interpreted as definitive evidence of caspase activation or apoptotic cell death.

Comparable pathway-associated changes were observed in MDA-MB-231 cells (Figure 4F-H, I). Ins/$CoCl_2$ stimulation increased mTOR fluorescence by approximately twofold and HIF-1α fluorescence by approximately threefold relative to untreated controls. TCS treatment significantly reduced both signals, restoring mTOR-associated fluorescence toward basal levels and markedly attenuating HIF-1α accumulation. Caspase-3 immunoreactivity increased following TCS treatment and reached approximately twofold above control in the Ins/$CoCl_2$ + TCS group.

Taken together, these immunocytochemical findings associate TCS treatment with attenuation of PI3K/AKT/mTOR-HIF-1α-related signaling and increased Caspase-3-associated staining in A549 and MDA-MB-231 cells. The results support a pathway-centered mechanistic hypothesis but require confirmation using phospho-specific immunoblotting, kinase or target-engagement assays, and direct measurements of caspase activation and apoptosis.

KEGG enrichment analysis of the predefined 12-gene set identified Apoptosis, PI3K–Akt signaling, HIF-1 signaling, p53 signaling, Autophagy, VEGF signaling, TNF signaling, JAK–STAT signaling, MAPK signaling, and mTOR signaling among the most significantly enriched pathways (Figure 5). These pathways encompass key biological processes associated with the selected target genes, including regulation of apoptosis, cell survival, proliferation, hypoxic adaptation, inflammatory signaling, angiogenesis, and cellular metabolism. Because the input gene set was selected based on prior biological knowledge and network analysis, the enrichment results should be interpreted as a functional characterization of the predefined targets rather than evidence of TCS-induced pathway regulation or treatment-driven pathway discovery.

# 4. Discussion

This study completes a critical step in the *A. eupatoria*-TCS research sequence. The earlier work established extract-level anticancer activity, identified TCS by LC-HRMS, and proposed it as a PI3K-targeting lead through docking. The present work directly tests the isolated compound and shows that TCS is biologically active in cancer cells. The strongest conclusion is therefore not that TCS explains the activity of AEE, but that a candidate first nominated from the extract exhibits reproducible, cell-context-dependent anticancer-associated phenotypes when evaluated independently.

The studies on MCF-7 breast cancer cells provide the clearest evidence of direct TCS activity. Reduced RTCA AUC together with increased E-Tox Green fluorescence and a marked shift toward dual-positive and green-dominant objects indicates suppression of cumulative cell growth/adhesion accompanied by membrane-compromise-associated cell death. MCF-7 cells are a luminal, hormone-receptor-positive model in which PI3K pathway dependence is common, and their sensitivity is consistent with the

pathway-centered hypothesis generated by the earlier AEE study. A recent study of maslinic acid similarly found greater 72 h sensitivity in MCF-7 than in MDA-MB-231 cells and linked the response to PI3K-AKT-mTOR and other cancer pathways [17]. This comparison does not imply a shared direct target, but it illustrates how natural-product responses can diverge across breast cancer subtypes.

The data obtained from MDA-MB-231 triple-negative breast cancer cells are equally informative because they prevent a simple classification of TCS as either cytotoxic or inactive. AEE significantly reduced proliferation-associated cell-index AUC, whereas TCS did not substantially alter the cumulative impedance signal. Nevertheless, TCS significantly reduced migration-associated impedance and produced a marked shift from the live-like quadrant toward dual-positive and green-dominant fluorescence populations. This discordance may reflect differences in what the assays measure: impedance integrates cell number, attachment, and morphology across the well, whereas object-level fluorescence classification emphasizes dye intensities among detected objects. The scatter categories are operational and do not by themselves establish apoptosis, but they indicate that TCS should not be described as lacking cytotoxicity-associated effects in this cell line. Orthogonal confirmation using flow cytometry, independent viability assays, and biochemical cell-death markers is therefore essential. Basal-like and triple-negative breast cancers also exhibit distinct polyamine and signaling dependencies; for example, AMD1-driven spermidine production and eIF5A hypusination can promote aggressive breast cancer behavior [10]. The present data concern hydroxycinnamoyl spermidine conjugate rather than free spermidine; nevertheless, together with emerging evidence on polyamine metabolism in cancer, they underscore the importance of cell-, context-, and assay-dependent interpretation of polyamine-related effects [10, 18].

The pathway-associated findings provide a coherent, but still provisional, mechanism. In A549 cells, TCS reduced pPI3K, pAKT, mTOR, and HIF-1α fluorescence under insulin/$CoCl_2$ stimulation; in MDA-MB-231 cells, it reduced mTOR and HIF-1α. This pattern is biologically consistent with established crosstalk in which PI3K/AKT/mTOR signaling promotes HIF-1α expression and metabolic adaptation (Tian et al., 2023; doi: 10.1038/s41523-023-00598-z). It also aligns with our earlier studies in which *A. eupatoria*, *Rumex obtusifolius*, and *Hypericum alpestre* preparations modulated PI3K/AKT-associated readouts in A549 and MDA-MB-231 models [6, 19, 20]. Nevertheless, ICC intensity is not equivalent to quantitative phosphoprotein analysis, and $CoCl_2$-induced HIF-1α stabilization is a chemical hypoxia model rather than physiological low oxygen. Western blotting, phospho-specific ELISA, kinase assays, and rescue experiments are needed to establish pathway causality.

The PPI and KEGG analyses placed the predefined target set within interconnected pathways involving PI3K-AKT-mTOR signaling, HIF-1, apoptosis, p53, autophagy, AMPK, glucose transport, migration, and inflammation. This convergence supports the biological plausibility of the selected marker panel and identifies testable downstream endpoints. Because the input genes were selected a priori, however, these analyses provide pathway contextualization rather than unbiased discovery or evidence that TCS transcriptionally regulates the enriched pathways.

Docking identified several plausible TCS-protein interaction hypotheses relevant to the observed phenotypes. Under the applied target-specific conditions, numerically more negative Vina scores were obtained for COX-2 and AKT, with an intermediate value for MMP-2. The predicted AKT and PI3K interactions are compatible with the observed PI3K/AKT/mTOR-associated changes, whereas MMP-2 and COX-2 provide potential links to migration- and inflammation-related processes. The weaker Bcl-2 and Caspase-3 predictions do not support attributing the increased Caspase-3-associated staining to direct TCS binding. These computational findings therefore identify candidate targets for biochemical and cellular target-engagement studies rather than establishing direct binding or a definitive target-preference hierarchy.

The comparison with prior TCS biology is also important. Zhou et al. reported that tricoumaroyl spermidine protected HepG2 cells against ethanol-induced apoptosis [9], whereas the present study observed cytotoxicity in MCF-7 cells and increased Caspase-3-associated staining under tumor-signaling stimulation. These findings are not necessarily contradictory. They indicate that TCS can be cytoprotective in one injury model and anticancer-associated in another, depending on cell lineage, stressor, concentration, exposure time, and signaling state. This context dependence should be emphasized as a central biological finding rather than treated as an inconsistency.

AEE and TCS produced partially overlapping but non-identical profiles. AEE strongly reduced MCF-7 endpoint viability and significantly reduced proliferation-associated impedance in MDA-MB-231 cells, whereas TCS showed stronger kinetic activity in MCF-7 cells and significant migration-inhibitory activity in MDA-MB-231 cells without a clear antiproliferative or cytotoxic effect.

Future studies. TCS remains an early-stage lead. Immediate priorities are to confirm its analytical identity, purity, stability, and intracellular exposure, evaluate selectivity in non-malignant cells, determine whether the MCF-7 phenotype reflects cell-cycle arrest, apoptosis, or another form of cell death; and validate the MDA-MB-231 migration phenotype using orthogonal migration, invasion, MMP, and epithelial-mesenchymal transition assays. Pharmacokinetic and in vivo studies should follow only after a preliminary therapeutic window and direct evidence of target engagement have been established.

# 5. Conclusions

This continuation study moves TCS from computational prioritization to direct cell-based validation. Isolated TCS showed an antiproliferative/cytotoxic phenotype in MCF-7 cells, no clear antiproliferative or cytotoxic effect but a significant reduction in migration-associated impedance in MDA-MB-231 cells, and pathway-associated suppression of PI3K/AKT/mTOR-HIF-1α signals with increased Caspase-3-associated staining under stimulated conditions. Docking, PPI, and KEGG analyses support a coherent multi-pathway hypothesis centered on PI3K/AKT/mTOR, HIF-1, apoptosis, and migration, but they do not establish direct target engagement. The data justify further development of TCS as a context-dependent natural-product lead while maintaining a clear distinction between compound activity and the activity of the chemically complex AEE.

# Abbreviations

AEE, *Agrimonia eupatoria* ethanolic extract; AKT/AKT1, AKT serine/threonine kinase (protein kinase B)/AKT serine/threonine kinase 1; AMD1, adenosylmethionine decarboxylase 1; AMPK, AMP-activated protein kinase; ANOVA, analysis of variance; ATCC, American Type Culture Collection; ATP, adenosine triphosphate; AUC, area under the curve; BAX, BCL2-associated X protein; BCL-2/BCL2, B-cell lymphoma 2; Caspase-3/CASP3, caspase 3; CASP9, caspase 9; CETSA, cellular thermal shift assay; CI, cell index; COX-2, cyclooxygenase-2; DAPI, 4',6-diamidino-2-phenylindole; DMEM, Dulbecco's modified Eagle's medium; eIF5A, eukaryotic translation initiation factor 5A; ERK, extracellular signal-regulated kinase; HIF-1α/HIF1A, hypoxia-inducible factor 1 alpha/hypoxia-inducible factor 1 subunit alpha; ICC, immunocytochemistry; JAK–STAT, Janus kinase–signal transducer and activator of transcription; KEGG, Kyoto Encyclopedia of Genes and Genomes; LC-Q-Orbitrap HRMS, liquid chromatography coupled to quadrupole-Orbitrap high-resolution mass spectrometry; MAPK, mitogen-activated protein kinase; MMP-2/MMP2, matrix metalloproteinase 2; MTT, 3-(4,5-dimethylthiazol-2-yl)-2,5-diphenyltetrazolium bromide; mTOR/MTOR, mechanistic target of rapamycin; NVP-BEZ235, dactolisib; PDB, Protein Data Bank; PI3K, phosphoinositide 3-kinase; PIK3CA, phosphatidylinositol-4,5-bisphosphate 3-kinase catalytic subunit alpha; PPI, protein–protein interaction; PTGS2, prostaglandin-endoperoxide synthase 2; ROS, reactive oxygen species; RTCA, real-time cell analysis; SD, standard deviation; SEM, standard error of the mean; SLC2A1, solute carrier family 2 member 1; STRING, Search Tool for the Retrieval of Interacting Genes/Proteins; TCF4, transcription factor 4; TCS, tricoumaroyl spermidine; TNF, tumor necrosis factor; TP53, tumor protein p53; VEGF, vascular endothelial growth factor.

# Declarations


### Acknowledgements

Plant material was identified by Dr. Narine Zakaryan from the Department of Botany and Mycology at Yerevan State University.


### Authors' contributions

All authors contributed to the study's conception and design. HJ, MK, AH, AG, and MG carried out the investigations and analyzed the outcomes. MG and NA wrote the manuscript. MG, NA, HJ, and AM directed the experiments, corrected, and edited the manuscript. All authors revised and accepted the final version of the manuscript.


### Funding

This work was supported by the Higher Education and Science Committee of MESCS RA Research projects numbered 23LCG-1F010 and 24WS-1F036.

### Data availability

The datasets and materials used and/or analyzed during the current study are available from the corresponding author upon reasonable request.

### Declarations

### Ethics approval and consent to participate

Not applicable with respect to human participants, human data or tissue, and animals, none of which were involved in this study. Aerial parts of *Agrimonia eupatoria* L. were collected on privately owned land near Navur village, Tavush region, Armenia, with the permission of the landowner. The collection of plant material complied with relevant institutional, national, and international guidelines and legislation. A voucher specimen (ERCB13207) was deposited in the Yerevan State University Herbarium.

### Consent for publication

All authors have read and approved the final manuscript.

### Competing interests

The authors declare no competing interests.

## References


1. Sung H, Filho AM, Laversanne M, Ferlay J, Siegel RL, Soerjomataram I, et al. Global cancer statistics 2024: GLOBOCAN estimates of incidence and mortality worldwide for 34 cancers in 186 countries. CA Cancer J Clin. 2026;76. https://doi.org/10.3322/caac.70090.
2. Glaviano A, Foo ASC, Lam HY, Yap KCH, Jacot W, Jones RH, et al. PI3K/AKT/mTOR signaling transduction pathway and targeted therapies in cancer. Mol Cancer. 2023;22:138. https://doi.org/10.1186/s12943-023-01827-6.
3. Tian Y, Zhao L, Gui Z, Liu S, Liu C, Yu T, et al. PI3K/AKT signaling activates HIF1α to modulate the biological effects of invasive breast cancer with microcalcification. NPJ Breast Cancer. 2023;9:93. https://doi.org/10.1038/s41523-023-00598-z.
4. Chen Z, Han F, Du Y, Shi H, Zhou W. Hypoxic microenvironment in cancer: molecular mechanisms and therapeutic interventions. Signal Transduct Target Ther. 2023;8:70. https://doi.org/10.1038/s41392-023-01332-8.
5. Malheiros J, Simões DM, Figueirinha A, Cotrim MD, Fonseca DA, Agrimonia eupatoria L. An integrative perspective on ethnomedicinal use, phenolic composition and pharmacological activity. J Ethnopharmacol. 2022;296. https://doi.org/10.1016/j.jep.2022.115498.
6. Ginovyan M, Gevorgyan S, Javrushyan H, Kusznierewicz B, Koss-Mikołajczyk I, Sahakyan N, et al. Inhibition of the PI3K signaling pathway in cancer cells by Agrimonia eupatoria L. ethanolic extract:

identification of tricoumaroyl spermidine as a potential PI3K inhibitor. BMC Complement Med Ther. 2026;26:41. https://doi.org/10.1186/s12906-025-05231-z.

7. Zhang X, Chen J, Xi B, Liu Y, Wang S, Gu L, et al. Agrimoniin is a dual inhibitor of < scp>AKT and <scp > ERK pathways that inhibit pancreatic cancer cell proliferation</scp >. Phytother Res. 2023;37:4076–91. https://doi.org/10.1002/ptr.7867.
8. Zhu X, Zhang Y, Wang Y, Zhang H, Wang X, Tang H, et al. Agrimoniin sensitizes pancreatic cancer to apoptosis through ROS-mediated energy metabolism dysfunction. Phytomedicine. 2022;96:153807. https://doi.org/10.1016/j.phymed.2021.153807.
9. Zhou Q, Wang L, Liu B, Xiao J, Cheng K-W, Chen F, et al. Tricoumaroylspermidine from rose exhibits inhibitory activity against ethanol-induced apoptosis in HepG2 cells. Food Funct. 2021;12:5892–902. https://doi.org/10.1039/D1FO00800E.
10. Liao R, Chen X, Cao Q, Bai L, Ma C, Dai Z, et al. AMD1 promotes breast cancer aggressiveness via a spermidine-eIF5A hypusination-TCF4 axis. Breast Cancer Res. 2024;26:70. https://doi.org/10.1186/s13058-024-01825-6.
11. Javrushyan H, Petrosyan G, Mróz M, Kusznierewicz B, Alharithi Y, Ginovyan M, et al. Evaluating the Efficacy of Polyphenol-Enriched Plant Extracts and Pathway Modulators in the Bone Marrow to Suppress Breast Cancer Progression. FASEB J. 2026;40. https://doi.org/10.1096/fj.202501773RRR.
12. Trott O, Olson AJ. AutoDock Vina: Improving the speed and accuracy of docking with a new scoring function, efficient optimization, and multithreading. J Comput Chem. 2010;31:455–61. https://doi.org/10.1002/jcc.21334.
13. Shannon P, Markiel A, Ozier O, Baliga NS, Wang JT, Ramage D, et al. Cytoscape: A Software Environment for Integrated Models of Biomolecular Interaction Networks. Genome Res. 2003;13:2498–504. https://doi.org/10.1101/gr.1239303.
14. Kanehisa M, Furumichi M, Sato Y, Kawashima M, Ishiguro-Watanabe M. KEGG for taxonomy-based analysis of pathways and genomes. Nucleic Acids Res. 2023;51:D587–92. https://doi.org/10.1093/nar/gkac963.
15. Lequeux A, Noman MZ, Xiao M, Sauvage D, Van Moer K, Viry E, et al. Impact of hypoxic tumor microenvironment and tumor cell plasticity on the expression of immune checkpoints. Cancer Lett. 2019;458:13–20. https://doi.org/10.1016/j.canlet.2019.05.021.
16. Wilson WR, Hay MP. Targeting hypoxia in cancer therapy. Nat Rev Cancer. 2011;11:393–410. https://doi.org/10.1038/nrc3064.
17. Tan SY, Foo CN, Ng FL, Tan CH, Lim YM. Gene Expression Profiling of Maslinic Acid-treated MCF-7 Breast Cancer Cells Using Nanostring nCounter Pancancer Pathway Panel. Gene. 2025;935:149043. https://doi.org/10.1016/j.gene.2024.149043.
18. Yerlikaya A. Polyamines in Cancer: Mechanisms, Metabolic Targets, and Therapeutic Opportunities. Anticancer Agents Med Chem. 2026;26:473–85. https://doi.org/10.2174/0118715206390332250711060007.

19. Ginovyan M, Javrushyan H, Hovhannisyan S, Nadiryan E, Sevoyan G, Harutyunyan T, et al. 5-fluorouracil and Rumex obtusifolius extract combination trigger A549 cancer cell apoptosis: uncovering PI3K/Akt inhibition by in vitro and in silico approaches. Sci Rep. 2024;14:14676. https://doi.org/10.1038/s41598-024-65816-5.
20. Javrushyan H, Ginovyan M, Harutyunyan T, Gevorgyan S, Karabekian Z, Maloyan A, et al. Elucidating the impact of Hypericum alpestre extract and L-NAME on the PI3K/Akt signaling pathway in A549 lung adenocarcinoma and MDA-MB-231 triple-negative breast cancer cells. PLoS ONE. 2025;20:e0303736. https://doi.org/10.1371/journal.pone.0303736.

# Figures

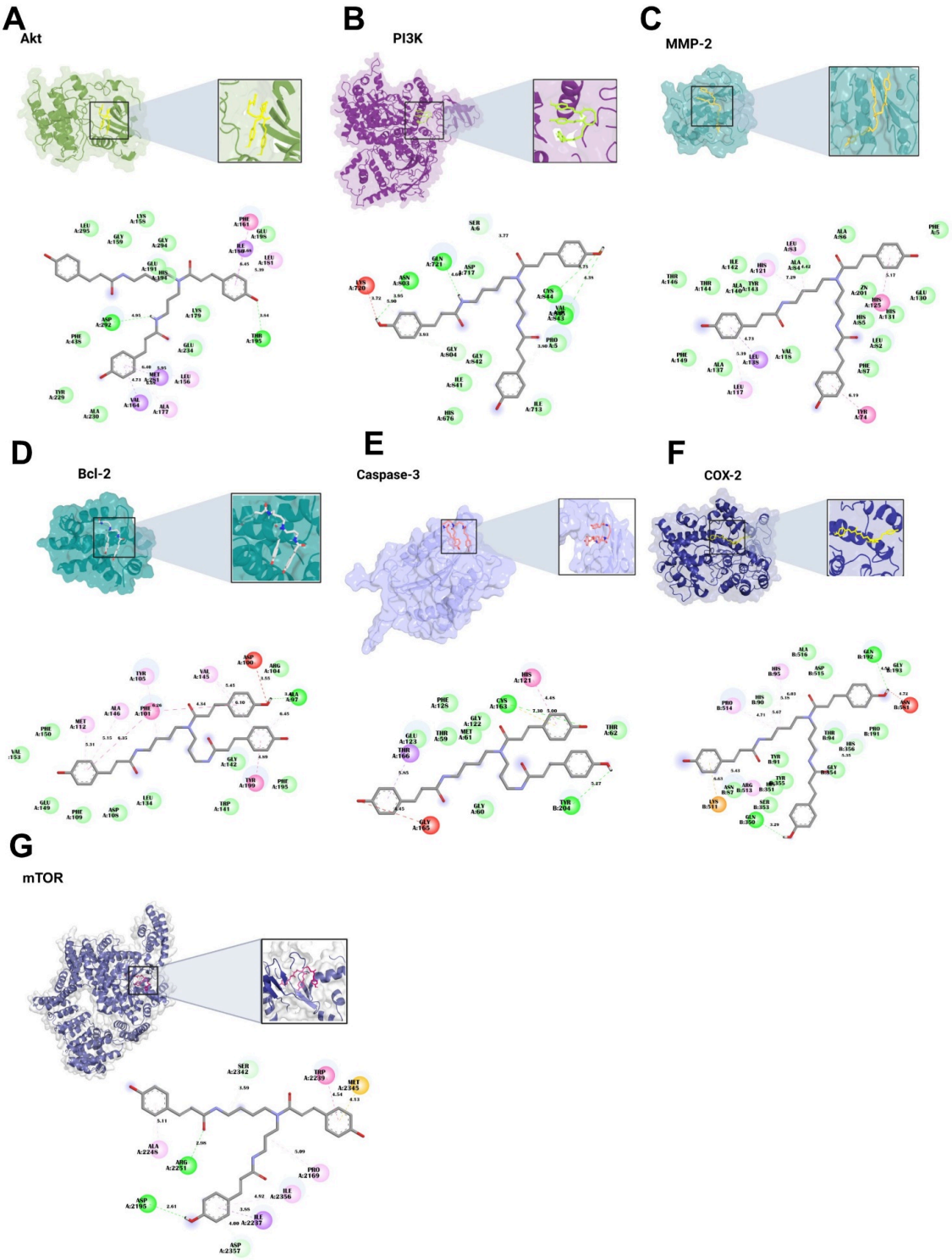


## Figure 1

**Predicted docking poses and interaction profiles of tricoumaroyl spermidine with six cancer-associated proteins.**(A) AKT, (B) PI3K, (C) MMP-2, (D) Bcl-2, (E) Caspase-3, (F) COX-2, and (G) mTOR. Each panel presents a three-dimensional docking pose and the corresponding two-dimensional non-covalent interaction map. The interaction diagrams depict the predicted molecular contacts between tricoumaroyl spermidine and amino acid residues within the respective protein-binding pockets.

AutoDock Vina scores were −8.483, −5.751, -8,395, −6.888, −5.061, −4.361, and −8.947 kcal/mol for AKT, PI3K, mTOR, MMP-2, Bcl-2, Caspase-3, and COX-2, respectively. Interaction types are color-coded as follows: green dashed lines indicate conventional hydrogen bonds; pale-green dashed lines indicate carbon-hydrogen bonds; purple dashed lines indicate π-sigma interactions; pink dashed lines indicate π-alkyl interactions; magenta dashed lines indicate π-π interactions, including stacked and T-shaped contacts; orange dashed lines indicate π-cation interactions; yellow dashed lines indicate π-sulfur interactions; red dashed lines indicate unfavorable contacts; and light-green residue labels indicate van der Waals interactions. Docking predictions are hypothesis-generating and do not establish direct binding or functional target engagement.

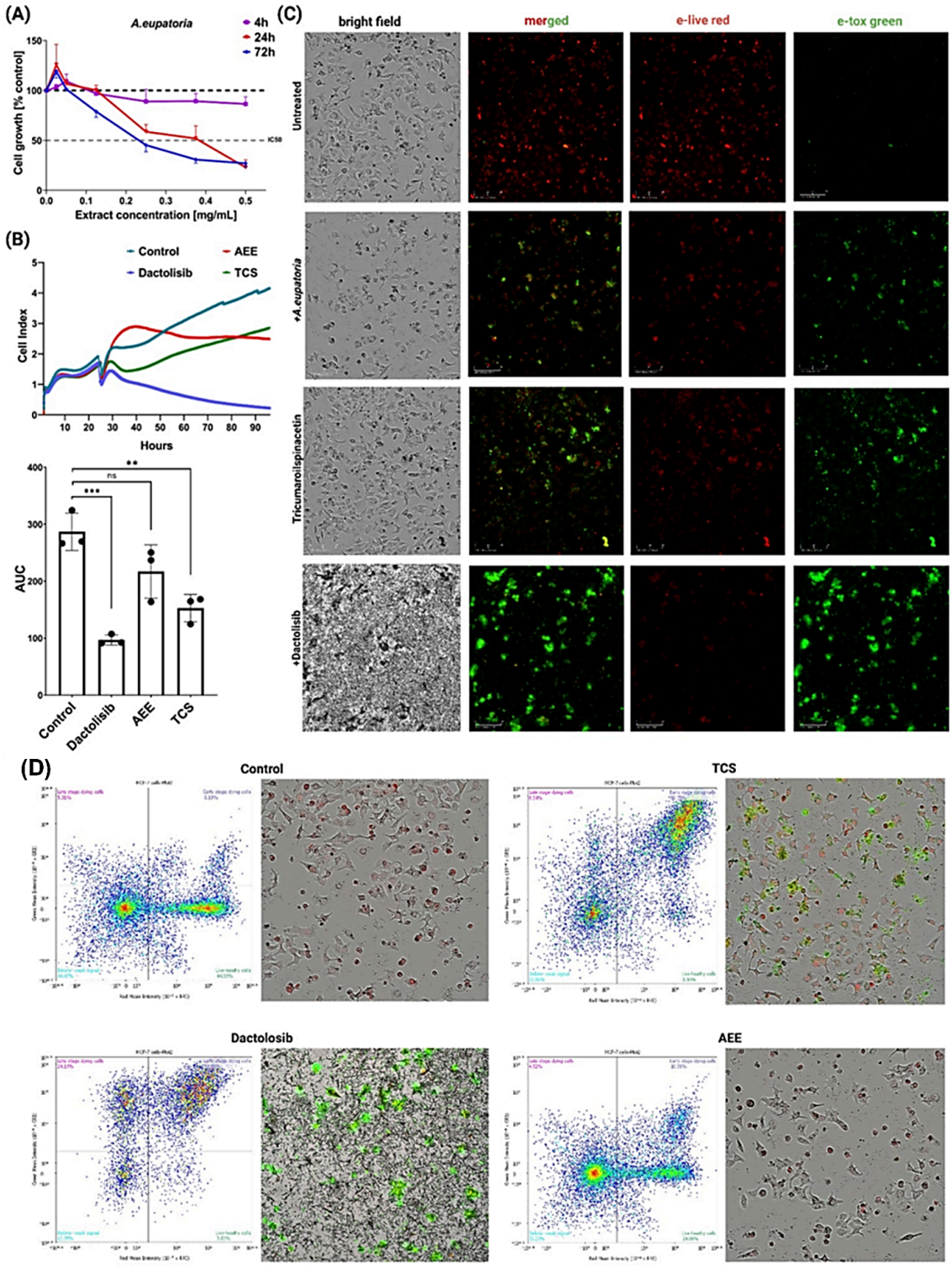


## Figure 2

**Antiproliferative and cytotoxic effects of *Agrimonia eupatoria* ethanolic extract and tricoumaroyl spermidine in MCF-7 breast cancer cells. (A)**Concentration- and time-dependent effects of *A. eupatoria* ethanolic extract (AEE; 0-0.5 mg/mL) on MCF-7 cell viability after 4, 24, and 72 h of exposure. Cell viability was expressed relative to the corresponding vehicle-treated control, defined as 100%. Horizontal dashed lines indicate 100% viability and the 50% response threshold. Data are presented as mean ± SEM

from three independent experiments. **(B)** Real-time impedance-based monitoring of MCF-7 cell behavior using the xCELLigence RTCA system. The upper panel shows cell-index kinetics for vehicle-treated control cells and cells treated with AEE (0.5 mg/mL), tricoumaroyl spermidine (TCS; 50 μM), or dactolisib (0.2 μM). The lower panel shows the corresponding area-under-the-curve analysis over the recorded monitoring interval. Data are presented as mean ± SD from three independent experiments, with individual experimental values shown. Statistical significance is indicated as **$p < 0.01$ and ***$p < 0.001$; ns, not significant. **(C)** Representative bright-field and fluorescence images of MCF-7 cells following 72 h of treatment with AEE (0.5 mg/mL), TCS (50 μM), or dactolisib (0.2 μM). E-Live Red staining indicates viable cells, whereas E-Tox Green staining identifies cells with compromised plasma-membrane integrity. Bright-field, merged fluorescence, E-Live Red, and E-Tox Green channels are shown for each treatment condition. Scale bars are indicated in the images. **(D)** Representative object-level bivariate scatter plots after 72 h of treatment. The x-axis shows E-Live Red mean intensity and the y-axis E-Tox Green mean intensity. Quadrants operationally denote Red+/Green− live-like objects, Red+/Green+ dual-positive objects, Red−/Green+ green-dominant objects, and Red−/Green− low-signal/debris. Percentages of total gated objects are shown within each quadrant. These fluorescence-defined categories do not establish stages of apoptosis. Plots are representative of three independent experiments.

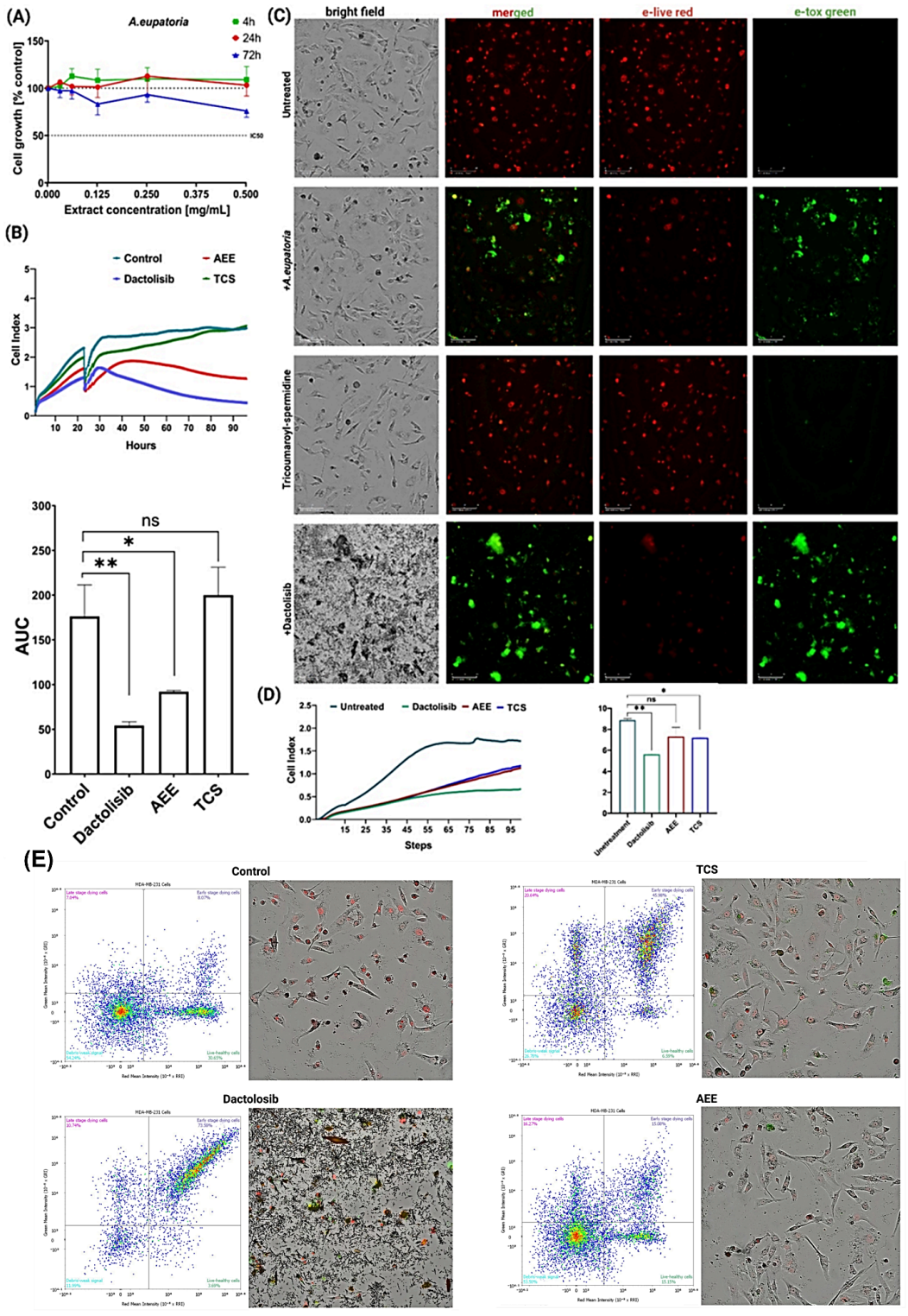


## Figure 3

**Antiproliferative, cytotoxicity-associated, and migration-associated effects of *Agrimonia eupatoria* ethanolic extract and tricoumaroyl spermidine in MDA-MB-231 triple-negative breast cancer cells.** **(A)**Concentration- and time-dependent effects of *A. eupatoria* ethanolic extract (AEE; 0-0.5 mg/mL) on MDA-MB-231 cell viability after 4, 24, and 72 h of exposure. Cell viability was expressed relative to the corresponding vehicle-treated control, defined as 100%. Horizontal dashed lines indicate 100% viability

and the 50% response threshold. Data are presented as mean ± SEM from three independent experiments. **(B)** Real-time impedance-based monitoring of MDA-MB-231 cell behavior using the xCELLigence RTCA system. The upper panel shows cell-index kinetics for vehicle-treated control cells and cells treated with AEE (0.5 mg/mL), tricoumaroyl spermidine (TCS; 50 μM), or dactolisib (0.2 μM) over the 96-h monitoring period. The lower panel presents the corresponding area-under-the-curve analysis. Dactolisib and AEE significantly reduced the proliferation-associated AUC relative to control, whereas TCS did not differ significantly from control. Data are presented as mean ± SD from three independent experiments. Statistical significance is indicated as $p < 0.05$; ns, not significant. **(C)** Representative bright-field and fluorescence images of MDA-MB-231 cells following 72 h of treatment with AEE (0.5 mg/mL), TCS (50 μM), or dactolisib (0.2 μM). E-Live Red staining indicates viable cells, whereas E-Tox Green staining identifies cells with compromised plasma-membrane integrity. Bright-field, merged fluorescence, E-Live Red, and E-Tox Green channels are shown for each treatment condition. Scale bars are indicated in the images. **(D)** Real-time impedance-based analysis of MDA-MB-231 cell migration using the xCELLigence RTCA DP system and CIM-Plate 16. The left panel shows migration-associated cell-index profiles for vehicle-treated control cells and cells treated with dactolisib (0.2 μM), AEE (0.5 mg/mL), or TCS (50 μM), recorded at 15-min intervals over 24 h. Control cells exhibited the highest migration-associated cell-index trajectory, whereas all treatment groups showed lower trajectories during the monitoring period. The right panel presents the corresponding area-under-the-curve analysis. AUC analysis confirmed a significant reduction in migration-associated impedance for TCS relative to control. (**E**) Representative object-level bivariate scatter plots after 72 h of treatment. The x-axis shows E-Live Red mean intensity and the y-axis E-Tox Green mean intensity. Quadrants operationally denote Red+/Green− live-like objects, Red+/Green+ dual-positive objects, Red−/Green+ green-dominant objects, and Red−/Green− low-signal/debris. Percentages of total gated objects are shown within each quadrant. These fluorescence-defined categories do not establish stages of apoptosis. Plots are representative of three independent experiments. Data are presented as mean ± SD from three independent experiments. Statistical significance is indicated as $p < 0.05$; ns, not significant.

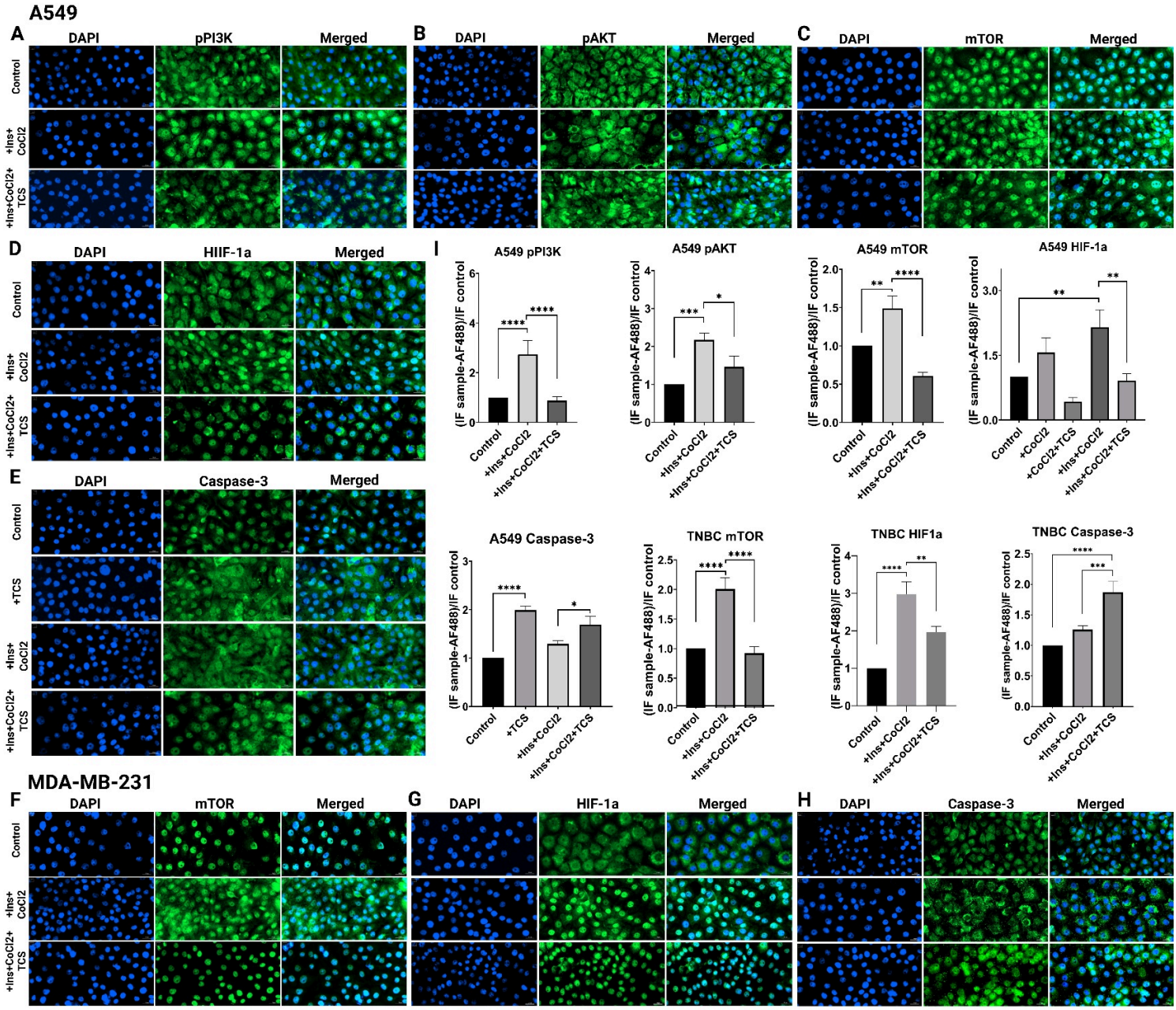


## Figure 4

**Immunocytochemical analysis of PI3K/AKT/mTOR signaling, HIF-1α expression, and Caspase-3-associated staining following tricoumaroyl spermidine treatment.** A549 and MDA-MB-231 cells were exposed to insulin (Ins, 200 nM) and cobalt chloride ($CoCl_2$, 200 μM) to mimic metabolic and hypoxia-associated conditions of the tumor microenvironment, followed by treatment with tricoumaroyl spermidine (TCS, 50 μM). In A549 cells, representative images and quantification are shown for pPI3K (A), pAKT (B), mTOR (C), HIF-1α (D), and Caspase-3 (E). In MDA-MB-231 cells, representative images and quantification are shown for mTOR (F), HIF-1α (G), and Caspase-3 (H). Immunocytochemical staining was performed using rabbit primary antibodies against the indicated targets at a dilution of 1:250, followed by Alexa Fluor 488-conjugated secondary antibody. Nuclei were counterstained with DAPI. Images were acquired at room temperature using a 20× objective; scale bar = 100 μm. For each

condition, eight fields of view per well were captured across three independent experiments (n = 3). Green fluorescence indicates target-protein immunoreactivity, and blue fluorescence indicates nuclear DAPI staining. Quantitative fluorescence intensities (I) were normalized to the untreated control group and are presented as mean ± SEM. Statistical significance is indicated as *p < 0.05, **p < 0.01, ***p < 0.001, and ****p < 0.0001.

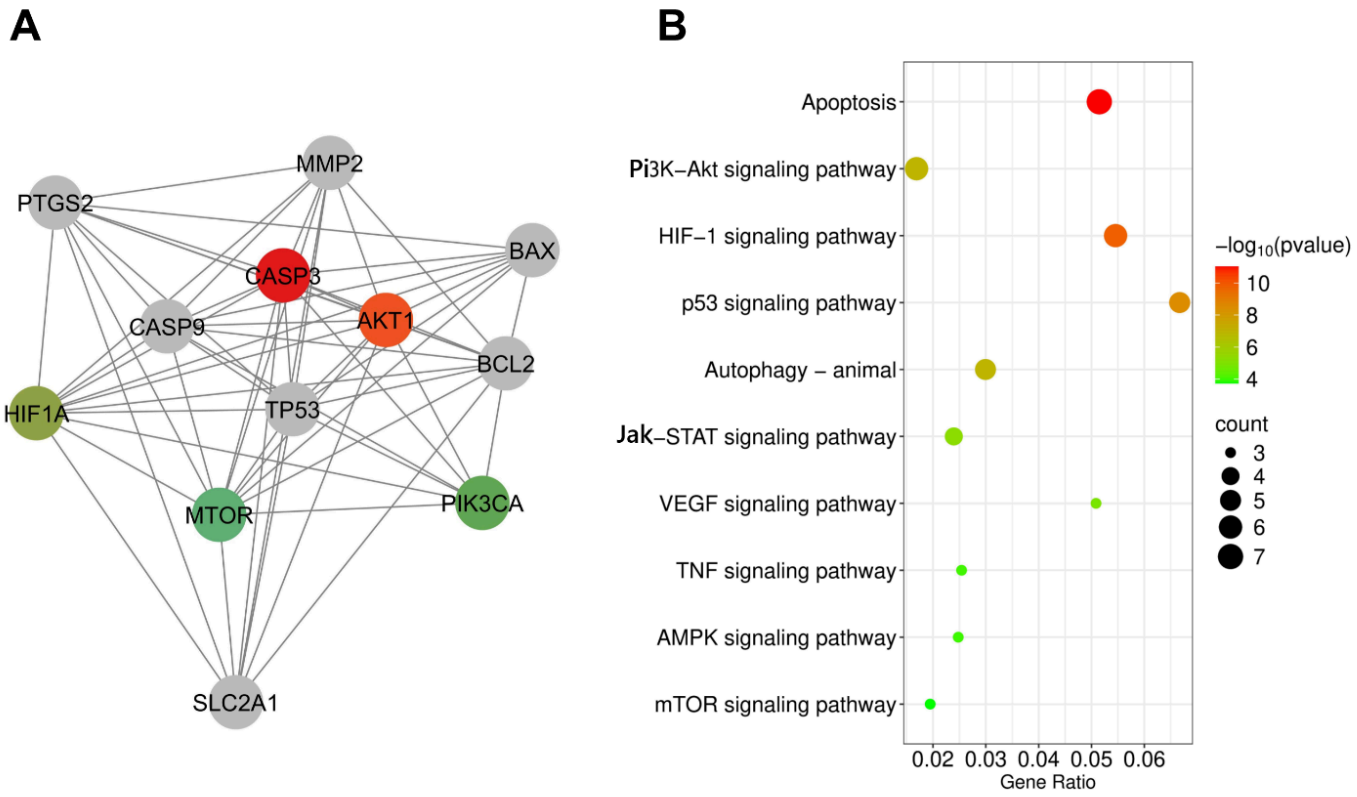


**Figure 5**

**Protein-protein interaction network and KEGG pathway enrichment of the candidate target set. (A)** Protein-protein interaction (PPI) network constructed using STRING v12.0 and visualized in Cytoscape v3.10.3. The seed proteins experimentally evaluated by immunocytochemistry—PIK3CA, AKT1, MTOR, CASP3, and HIF1A—are shown as colored nodes. Gray nodes represent additional functionally associated proteins identified through STRING network expansion, including TP53, CASP9, BAX, BCL2, PTGS2, MMP2, and SLC2A1. Edges indicate known or predicted functional associations between proteins.

**(B)** Bubble plot of KEGG 2026 Human pathway enrichment analysis for the selected gene set comprising PIK3CA, AKT1, CASP3, HIF1A, MTOR, TP53, BCL2, BAX, CASP9, MMP2, SLC2A1, and PTGS2. The x-axis represents the gene ratio, the y-axis lists the enriched KEGG pathways, bubble size corresponds to the number of input genes mapped to each pathway, and bubble color indicates enrichment significance expressed as $-\log_{10}$(P value). The displayed pathways include Apoptosis, PI3K–Akt signaling, HIF-1 signaling, p53 signaling, Autophagy, VEGF signaling, TNF signaling, JAK–STAT signaling, MAPK signaling, and mTOR signaling, representing key biological processes associated with the selected target

genes. These analyses were performed to contextualize the predefined target set and should not be interpreted as evidence of TCS-induced transcriptional or pathway regulation.

## Supplementary Files

This is a list of supplementary files associated with this preprint. Click to download.

- image1.jpeg